

This is the peer reviewed version of the following article: Han, J., Lian, H., Cheng, X., Dong, Q., Qu, Y., & Wong, W. Y. (2021). Study of electronic and steric effects of different substituents in donor–acceptor molecules on multilevel organic memory data storage performance. *Advanced Electronic Materials*, 7(4), 2001097, which has been published in final form at <https://doi.org/10.1002/aelm.202001097>. This article may be used for non-commercial purposes in accordance with Wiley Terms and Conditions for Use of Self-Archived Versions.

Study of electronic and steric effects of different substituents in donor-acceptor molecules on multilevel organic memory data storage performance

Jinba Han, Hong Lian, Xiaozhe Cheng, Qingchen Dong*, Yongquan Qu, and Wai-Yeung Wong*

Jinba Han, Hong Lian, Xiaozhe Cheng, Prof. Qingchen Dong, Prof. Yongquan Qu
MOE Key Laboratory of Interface Science and Engineering in Advanced Materials, Taiyuan
University of Technology, 79 Yingze West Street, Taiyuan, 030024, P.R. China.
E-mail: dongqingchen@tyut.edu.cn

Xiaozhe Cheng, Prof. Wai-Yeung Wong
Department of Applied Biology and Chemical Technology, The Hong Kong Polytechnic
University (PolyU), Hung Hom, Hong Kong, P.R. China.
E-mail: wai-yeung.wong@polyu.edu.hk

Prof. Wai-Yeung Wong
PolyU Shenzhen Research Institute, Shenzhen 518057, P.R. China.

Keywords: organic resistive memory, WORM, donor-acceptor molecule, multilevel memory, trap depth

To study the influence of different types of substituent moieties onto the molecular backbones of conjugated donor-acceptor (D-A) molecules on the thin-film morphology and performance of their memory devices, three new molecules X-TBT were synthesized, which consist of the same backbone of two triphenylamine (T) groups and benzothiadiazole (BT) group, but have different substituents (X) with different electronic effects, i.e. cyano group (CN), *tert*-butyl group (^tBu), and methoxy group (OMe). Nonvolatile ternary write-once-read-many-times (WORM) data storage behavior is achieved for the CN-TBT and ^tBu-TBT based devices as compared to the binary memory characteristic of TBT (X = H). In contrast, OMe-TBT based device still maintains binary WORM behavior due to its unfavorable molecular packing motif and weak intermolecular charge transfer effect, but exhibits the lowest operating voltage (1.4 V) as a result of the lowest energy barrier between electrode and active layer. Notably, ^tBu-TBT based device displays the highest $I_{ON2}/I_{ON1}/I_{OFF}$ ratio of $10^7:10^3:1$. Altering the substituents in D–A molecules can adjust the molecular packing, thin film morphology and

electron trap depth of active layer, which then significantly influence the memory performances.

1. Introduction

Organic-based resistive memory devices are explored on the basis of resistance switching effect, which have been developed rapidly and also attracted considerable attention over the last decade in meeting the ever-growing demand of ultrahigh density data storage, flexible memory and in-memory computing, etc.^[1-8] To date, a wide variety of organic materials, such as the conjugated polymers, polymer-based nanocomposites, and polymer-based electrets, have been extensively explored to develop high duty nonvolatile memory devices with fast switching speeds, reliable data storage and long retention time.^[9,10] It was reported recently that, by using the composite of [6,6]-phenyl C61-butyric acid methyl ester and polyvinyl pyrrolidone as active layer materials, the device exhibits a typical nonvolatile write-once-read-many-times (WORM) storage effect with multistate resistive switching characteristic due to the formation and breaking of carbon-rich conducting filament.^[11] In addition, organic small-molecule materials, due to their tunable structures, high purity, low cost, good stimuli-responsive properties and solution processability have been widely studied and shown rich and adjustable resistive switching memory behaviors.^[12-17] At present, most of the research works are mainly focused on exploring materials with multilevel resistance switching properties and disclosing the device operating mechanism or the relationship between the molecular structure and memory behaviors.^[18-20] Lu's group has explored many D-A type resistance switching organic molecules and made important contribution in the development of high performance organic memory devices. For example, in 2013, Lu's group reported three TPA-based donor-acceptor (D-A) molecules with different electron-accepting groups.^[21] It is found that, by varying the electron-withdrawing strength of groups, the film morphology and electric performances of the active layers can be modulated, thereby

realizing ternary memory behavior. Then in 2016, the same group reported the NONIBTDT molecule consisting of two electron-donating groups (thiophene and carbazole groups) and three electron-withdrawing groups (1,8-naphthylimine (NI), benzothiadiazole (BT) and nitro (NO_2) groups), and successfully achieved the quaternary organic memory.^[22] It is believed that the quaternary storage behavior is achieved by three charge transfer processes, that is, the transfer of electrons from donor thiophene to acceptors BT, NI, and NO_2 in sequence. Generally, most of these works focused on the investigation of the influence of conjugated length, number and electron-withdrawing strength of acceptor moieties on the memory performance. However, the influence of electronic and steric effects of terminal groups of D–A small molecules on the device performance are rarely studied.^[23,24] A deep understanding of the electronic and steric effects of terminal groups on the memory device performance is essential for the rational design and development of novel D-A type resistance switching organic molecules. Also, it is still not very clear about the inter-relationship of the electronic effects of electron-donating and electron-withdrawing groups in realizing the multilevel data storage performance, because sometimes the ternary memory behavior cannot be achieved by introducing two different electron-withdrawing groups.^[25] It is generally accepted that donor groups can increase the highest occupied molecular orbital (HOMO) level, while acceptors can decrease the lowest unoccupied molecular orbital (LUMO) level.^[26] Introducing the strong electron-withdrawing groups usually causes higher energy barrier between ITO and organic semiconductors, resulting in the higher threshold voltage (V_{th}). On the contrary, when introducing the weaker electron-withdrawing groups, most devices exhibited volatile characteristics due to the shallower trap depth.^[21] Therefore, there is an urgent need but it is still a significant challenge to make a balance between threshold voltage and electric memory behavior. To the best of our knowledge, there is rarely a study on the influence of electronic and steric effects of terminal groups of D–A small molecules on their corresponding memory behavior. In this work, to gain a deeper understanding of the relationship between electronic

and steric effects of terminal groups and the electric memory properties of the target molecules, we chose the molecule of 4,4'-(benzo[c][1,2,5]thiadiazole-4,7-diyl)bis(N,N-diphenylaniline) (TBT) as the model compound due to its intramolecular charge transfer (ICT) character and flexible structural adjustability,^[27] and select the -CN, -^tBu and -OMe as terminal modifying units because of the following reasons: (i) the CN unit possesses a strong electron-withdrawing effect and good planarity due to its carbon–nitrogen triple bond;^[28] (ii) ^tBu is an electron-donating group with large steric effect which would be beneficial for edge-to-face π - π stacking interactions;^[29] (iii) OMe is also a strong electron-donating substituent and conducive to hole transport, which could be introduced to modify the energy levels and electrical conductivity of organic semiconductors.^[30] Then, three conjugated D-A type small molecules were explored and referred as CN-TBT, ^tBu-TBT and OMe-TBT, respectively. The results demonstrate that the introduction of -CN, -^tBu and -OMe moieties can effectively optimize the thin film morphology and the trap depth of molecules. The memory devices based on CN-TBT and ^tBu-TBT exhibit excellent nonvolatile ternary WORM memory behavior, while the model compound TBT and OMe-TBT based devices show binary WORM memory characteristic. Meanwhile, the ^tBu-TBT based device possesses the highest $I_{ON2}/I_{ON1}/I_{OFF}$ ratio and low switching threshold voltages, which is promising for practical memory application with low-power-consumption and high capacity. The difference in performances of these D-A molecules could mainly be attributed to the different trap depth and the variation in thin film morphological structure and molecular energy levels. We believe that this approach will promote the development of high-performance materials for practical memory applications.

2. Results and discussion

2.1. Synthesis and characterization

The chemical structures and detailed synthetic routes of target molecules are shown in **Figure 1** and **Scheme S1**. The model compound TBT was synthesized according to the previously reported procedure.^[31] Three key intermediates 4,4'-((4-iodophenyl)azanediyl)dibenzonitrile (CN-TPA-I), 4,4'-((4-iodophenyl)methylene)bis(*tert*-butylbenzene) (^tBu-TPA-I), and 4-iodo-N,N-bis(4-methoxyphenyl)aniline (OMe-TPA-I) were synthesized by Ullmann coupling reaction and free radical substitution reaction, respectively. The target molecules CN-TBT, ^tBu-TBT, and OMe-TBT were synthesized by the palladium catalyzed Suzuki coupling reaction of CN-TPA-I, ^tBu-TPA-I, OMe-TPA-I and BPIN-BT, and then purified by column chromatography to give rise to CN-TBT, ^tBu-TBT, and OMe-TBT with yields of 47%, 29% and 22%, respectively. The chemical structures of all final products were characterized and confirmed by ¹H NMR, ¹³C NMR, and MALDI-TOF MS, respectively (see **Figures S1-S12**). The FT-IR spectra show characteristic absorption bands at around 2222 cm⁻¹ (CN) for CN-TBT, 1361 cm⁻¹ (C–H) for ^tBu-TBT, and 1240 cm⁻¹ (C–O) for OMe-TBT (**Figure S13**), which further verify that the chemical structures of as-synthesized compounds are consistent with the target ones.

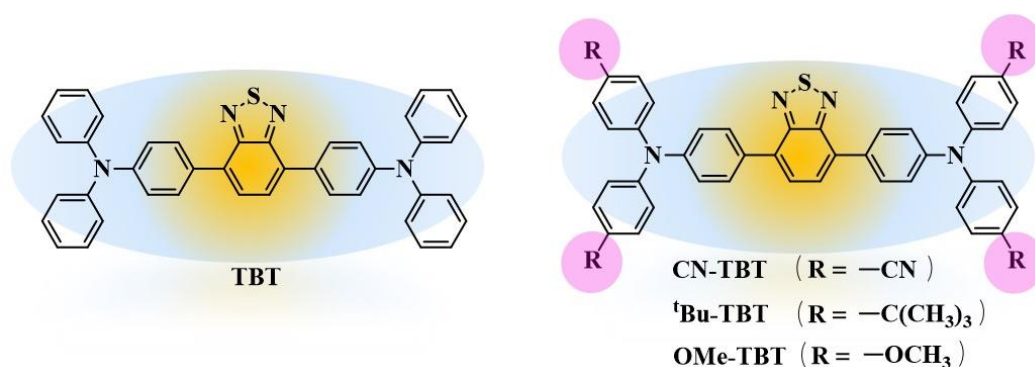


Figure 1 Molecular structures of TBT, CN-TBT, ^tBu-TBT, and OMe-TBT.

2.2. Thermal properties

The thermal properties of compounds TBT, CN-TBT, ^tBu-TBT, and OMe-TBT were characterized by TGA and DSC under a nitrogen atmosphere. As observed in the TGA curves in **Figure 2a**, the onset decomposition temperature (*T*_d, corresponding to 5% weight loss) of

TBT, CN-TBT, ^tBu-TBT, and OMe-TBT are 412.6 °C, 473.6 °C, 454.5 °C and 417.1 °C, respectively, implying a good thermal stability of the as-deposited active layers in the following memory devices. From the DSC curves in **Figure 2b**, we can see that the glass transition temperature (T_g) of TBT, CN-TBT, ^tBu-TBT and OMe-TBT are 97.2 °C, 147.3 °C, 151.7 °C and 93.6 °C, respectively. The relatively higher T_d and T_g of CN-TBT and ^tBu-TBT is mainly due to their more rigid structure and specific intermolecular interaction. It is noteworthy that ^tBu-TBT has the highest melting point (T_m) and the highest T_g due to the unique molecular interaction and packing mode resulting from the steric effect of ^tBu moiety, which coincided with that obtained by Grazulevicius and coworkers.^[32] As depicted in **Figure S14**, TBT can be fully crystallized at 176.6 °C exhibiting a sharp exothermic peak, while ^tBu-TBT is partially crystallized at 227.5 °C, indicating that TBT and ^tBu-TBT tend to crystallize during evaporation and deposition processes.^[27] The TGA and DSC data demonstrate that these molecules have good thermal stability in resisting the inevitable joule heat during the course of device operation, and therefore are ideal materials for memory devices.

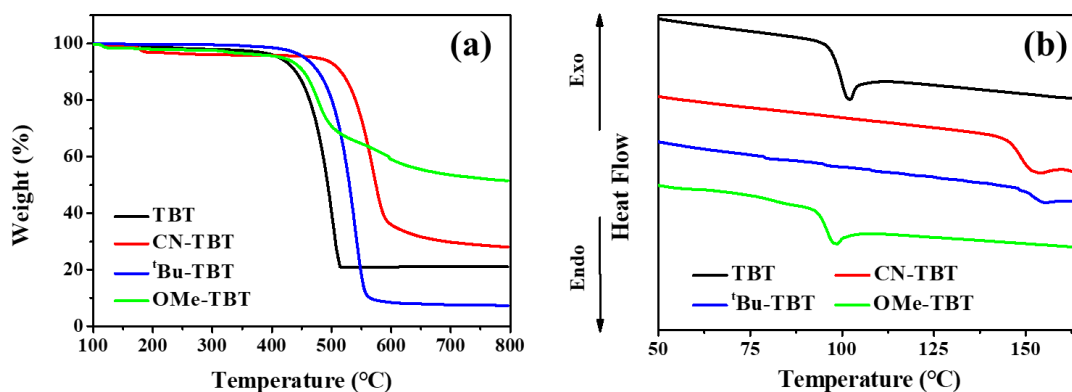


Figure 2 (a) TGA curves and (b) DSC thermograms of TBT, CN-TBT, ^tBu-TBT, and OMe-TBT with a heating rate of 10 °C/min under a nitrogen atmosphere.

2.3. Photophysical properties

To investigate the effects of different substituents on the photophysical properties of molecules, UV-vis absorption spectra (at room temperature in THF) of TBT, CN-TBT, ^tBu-TBT and OMe-TBT were measured and presented in **Figure 3**. The UV-vis absorption

spectra of these molecules demonstrate two dominant absorption bands: the former one located at 310-325 nm was derived from the $\pi \rightarrow \pi^*$ transition of TPA moiety and the latter at 420-500 nm can be attributed to the ICT interaction between the TPA unit and BT unit in the main chain.^[33, 34] Compared to TBT, ^tBu-TBT and OMe-TBT, the absorption peak of CN-TBT at 320 nm was red shifted, which is mainly due to the elongation of π conjugation, making $\pi \rightarrow \pi^*$ transition more effective in the D-A system.^[35] In addition, CN-TBT displays a strong absorption peak at 344 nm, as a result of the CT transition from TPA unit to CN unit.^[36]

It can be observed that with the strength of the electron-donating ability of substituents increased, the CT transition peaks are red-shifted. Hence, the corresponding optical band gap is decreased with the E_g of 2.32, 2.53, 2.25 and 2.18 eV for TBT, CN-TBT, ^tBu-TBT and OMe-TBT, respectively. The fluorescence spectra and photos under UV light and daylight can also directly manifest the influence of three substituents on the optical bandgaps of compounds. As seen from **Figure 3** (inset) and **Figure S15**, the colors of TBT, CN-TBT, ^tBu-TBT and OMe-TBT change from bright yellow to deep red (565 nm–636 nm) under the irradiation of UV (365 nm) lamp. As shown in Figure 3 and **Table S1**, the absorption bands of all compounds in film states show a noteworthy red-shift compared with their solution states, which indicated that ordered intermolecular π - π stacking or π -stacked aggregates with a *J*-type parallel stacking mode were formed in thin films of these compounds.^[38]

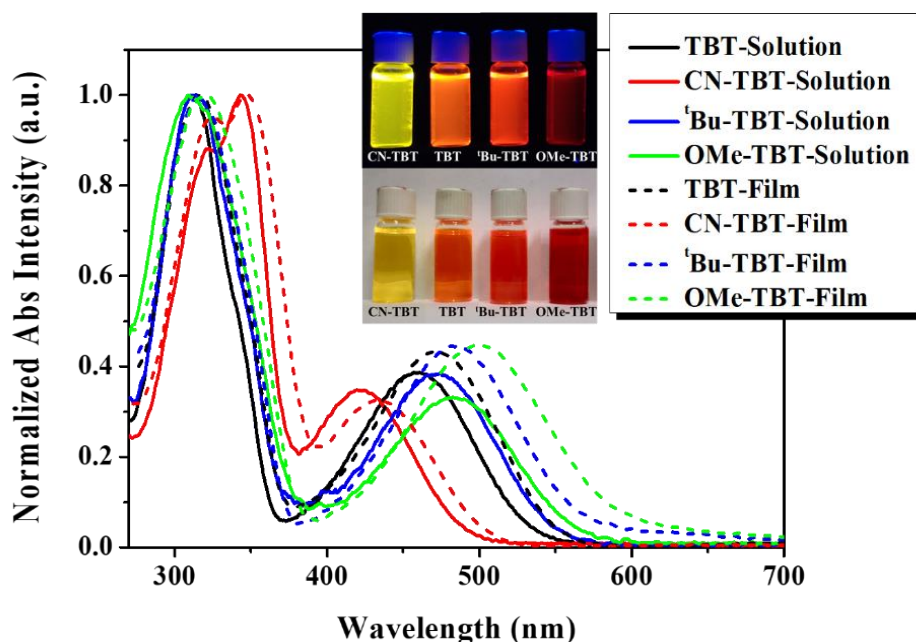


Figure 3 UV-vis absorption spectra of TBT, CN-TBT, ^tBu-TBT, and OMe-TBT in THF with concentration of 1.0×10^{-5} mol/L and thin film state (inset: the photos of CN-TBT, TBT, ^tBu-TBT, and OMe-TBT in THF with concentration of 1.0×10^{-3} mol/L under UV light and

2.4. Electrochemical properties

In order to further explore the electrochemical properties of these molecules with different terminal groups, the cyclic voltammograms (CVs) were obtained to determine the highest occupied molecular orbital (HOMO) and lowest unoccupied molecular orbital (LUMO) energy levels (**Figure 4a**). The CVs of TBT, CN-TBT, ^tBu-TBT, and OMe-TBT were measured in CH₃CN solution (0.1 M TBAPF₆ as the supporting electrolyte; scan rate: 100 mV/s), with SCE as reference electrode (ferrocenium/ferrocene (Fc/Fc⁺) redox couple was used as the standard, **Figure S16**), glassy-carbon electrode as working electrode and platinum-wire as counter electrode. The HOMO values of TBT, CN-TBT, ^tBu-TBT, and OMe-TBT are calculated to be -5.35, -5.60, -5.22 and -5.08 eV, respectively, by estimation from the onset oxidation potentials. The LUMO energy levels of these molecules are then calculated to be -3.03, -3.07, -2.97, -2.90 eV, respectively (as listed in **Table1**). It can be

learnt obviously from **Table 1** that the HOMO and LUMO energy levels are lifted with the electron-donating ability of substituents increased, but decreased with increasing the electron-withdrawing ability of substituents.^[39] The similar tendency is also obtained from the DFT theoretical calculation as discussed below. Thus, the trap depth of D–A small molecules can be effectively tuned through the introduction of different terminal substituents. As shown in **Figure 4b**, it is obvious that energy barriers between the work function of ITO electrode and organic semiconductors (0.55, 0.80, 0.42 and 0.28 eV for TBT, CN-TBT, ^tBu-TBT and OMe-TBT, respectively) is smaller than that between the work function of Al cathode and organic semiconductors (1.27, 1.23, 1.33 and 1.40 eV for TBT, CN-TBT, ^tBu-TBT and OMe-TBT, respectively), indicating that the hole injection is more favorable than electron injection and thus dominates the conduction process.

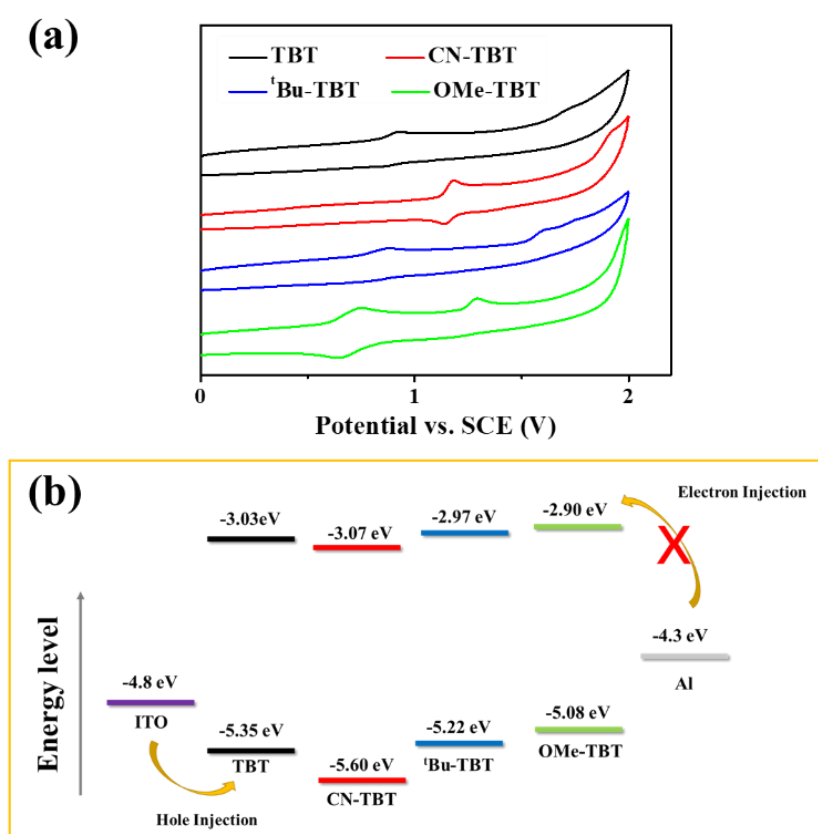


Figure 4 (a) The CV curves of TBT, CN-TBT, ^tBu-TBT, and OMe-TBT in 0.1 M TBAPF₆/CH₃CN solution and (b) Energy level diagram of the HOMO and LUMO for the D–A molecules along with the work function of the electrodes.

Table 1 Optical and electrochemical properties of the synthesized molecules.

Molecules	λ_{onset}^a (nm)	E_{ox}^b (V)	E_g^c (eV)	HOMO ^d (eV)	LUMO ^d (eV)
TBT	534	0.87	2.32	-5.35	-3.03
CN-TBT	490	1.12	2.53	-5.60	-3.07
^t Bu-TBT	552	0.74	2.25	-5.22	-2.97
OMe-TBT	568	0.60	2.18	-5.08	-2.90

^a Measured in THF.^b Measured from cyclic voltammetry.^c Estimated from onset of the absorption spectra ($E_g=1240/\lambda_{onset}$).^d Measured *versus* ferrocene, the HOMO and LUMO energy levels were determined using the following equations: $E_{HOMO} = [E_{ox} - E_{fc} + 4.8]$, $E_{LUMO} = [E_{HOMO} - E_g]$.

2.5. Organic memory behaviors

The resistor-type memory devices of the above D-A molecules were fabricated in a simple sandwich configuration comprising a pair of electrodes and a layer of small molecules (ITO/active layer/Al), as shown in **Figure 5a**. **Figure 5(b-e)** shows the typical *I*–*V* characteristics of these memory devices. Obviously, with the introduction of substituents (CN-TBT, ^tBu-TBT and OMe-TBT), the data storage behavior of memory devices for the CN-TBT and ^tBu-TBT based devices changes from binary WORM storage of TBT to ternary WORM storage, while the OMe-TBT based device still shows binary WORM data storage behavior. The *I*–*V* characteristic of devices based on TBT in **Figure 5b** shows two remarkable conductivity states. At first, the device based on TBT was in a low-conductivity state (OFF). As the positive bias increased, a sharp increase in current (i.e., 10^{-5} to 10^{-2} A) was observed at 1.7 V (sweep 1), which indicates a transition from the low-conductivity state (OFF) to the high-conductivity state (ON) with an ON/OFF current ratio of 10^3 . This electrical transition is regarded as the “writing” process for the memory device. After turning off the power or

applying the same direction scan voltage from 0 to 4 V (sweep 2) and reversed scan from 0 to -4 V (sweeps 3 and 4), the device still maintains the high-conductivity state. The sweep 5 (0 to 4 V) was conducted to reconfirm that the ON state of the device was continuously maintained. Therefore, the memory device based on TBT is a binary WORM data storage device.

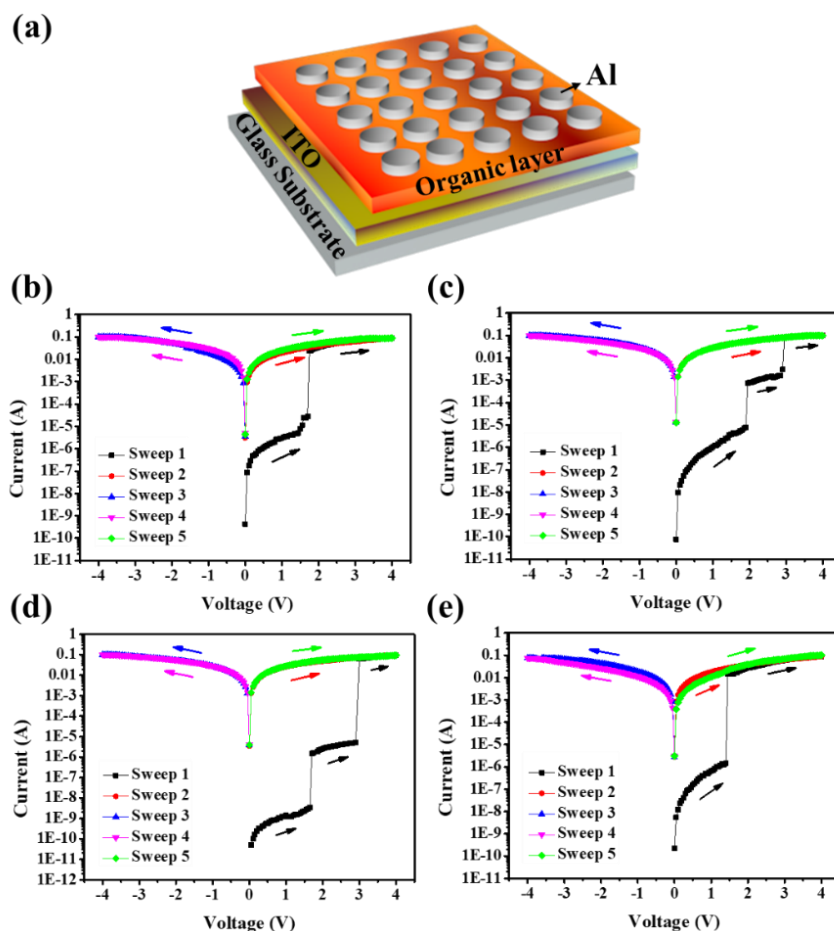


Figure 5 (a) Illustration of the sandwich memory device of the ITO/molecule/Al. I - V curves of the memory devices based on ITO/molecule/Al, (b) TBT, (c) CN-TBT, (d) t -Bu-TBT, and (e) OMe-TBT, respectively.

The I - V characteristic of the ITO/CN-TBT/Al device is shown in **Figure 5c**. When the positive bias from 0 V to 4V was applied onto the device, two abrupt increases in conductivity at the threshold voltages of around 1.9 V (ON1) and 2.9 V (ON2) were observed, indicating the existence of electrical tristable states. After a subsequent scan from 0 to 4 V (sweep 2), the storage cell remained at its high-conductivity state. Even when turning off the power or

applying a reverse voltage from 0 to -4 V was applied, the cell remained at its high-conductivity state (sweeps 3 and 4). The sweep 5 (0 to 4 V) was also performed to reconfirm the continuous maintenance of ON state. The current ratio of “ON2”, “ON1” and “OFF” states is $10^4:10^2:1$. This device, therefore, exhibited a typical ternary WORM memory behavior.

The I - V characteristics of memory devices based on ^tBu-TBT and OMe-TBT in the same conditions are shown in **Figure 5(d and e)**. For ^tBu-TBT based device, it exhibits the ternary WORM memory behavior similar to the CN-TBT. The threshold voltages are $V_{th1} = 1.7$ V and $V_{th2} = 2.9$ V, respectively, and the current ratio of “ON2”, “ON1” and “OFF” states is $10^7:10^3:1$ for the ^tBu-TBT based device. The relatively high current ratios are crucial for the device to realize low misreading probability and high-resolution in data access.^[40] For the OMe-TBT based device, it maintains the binary WORM memory behavior with the threshold voltage of $V_{th} = 1.4$ V and the ON/OFF current ratio of $10^4:1$. It is noteworthy that the V_{th} value of OMe-TBT based device is lower than that of other devices, which can be attributed to the lowest energy barrier between ITO and organic active layer. The higher ON/OFF ratio of OMe-TBT than TBT is ascribed to the stronger electron-donating ability of -OMe functional group. Moreover, the V_{th} values of CN-TBT, ^tBu-TBT and OMe-TBT based devices decrease in the order of CN-TBT > ^tBu-TBT > OMe-TBT, resulting from the difference of thin film morphological structure and trap depth. The device parameters of all devices are summarized in **Table 2**.

Table 2 A summary of device parameters of all devices.

Devices	TBT	CN-TBT	^t Bu-TBT	OMe-TBT
V_{th1} (V)	1.7	1.9	1.7	1.4
V_{th2} (V)	—	2.9	2.9	—

ON/OFF current ratio	$10^3:1$	$10^4:10^2:1$	$10^7:10^3:1$	$10^4:1$
----------------------	----------	---------------	---------------	----------

Considering that the memory behavior is closely related to the thickness of thin film, we then investigated the memory performances of ^tBu-TBT based devices with different thicknesses of active layers. The thickness of the ^tBu-TBT layer ranges from 50 to 500 nm, as shown in **Figure S17**. Interestingly, distinct switching behaviors can be found for devices based on ^tBu-TBT. For the device with 50 nm thick of ^tBu-TBT, no memory behavior was observed. The optimal device performance was obtained for ^tBu-TBT with the film thickness of 100 nm, achieving the lowest threshold voltages ($V_{th1} = 1.8$ V and $V_{th2} = 3.2$ V) and highest current ratio of "ON2", "ON1" and "OFF" states ($10^6:10^3:1$). Subsequently, the ternary memory behaviors remained for the devices based on ^tBu-TBT, but the performances (V_{th} , I_{ON}/I_{OFF} ratio) of which decreased gradually as the active layer thickness further increased to 150 and 250 nm. However, the memory behavior changed to the typical binary WORM type when the active layer thickness reaches up to 350 nm. The resistance switching behavior eventually disappeared as the film thickness increased to 500 nm. This is because the infused charge carriers could not effectively pass through the ^tBu-TBT film when the thickness increases to a certain level, thereby leading to the disappearance of the storage behavior of device.^[41] To investigate the cell-to-cell uniformity, we randomly selected 50 memory cells based on TBT, CN-TBT, ^tBu-TBT and OMe-TBT, and the statistical analysis of the data is shown in **Figure S18**. It was found that the yields of TBT and OMe-TBT based binary memory devices are 80% and 88%, respectively. Only 56% cells showed ternary WORM memory behavior for CN-TBT based devices, while for ^tBu-TBT, the yield increased up to 64%. We speculate that this might be due to the fact that the steric effect of *tert*-butyl groups can reduce the surface root-mean-square (RMS) of ^tBu-TBT active layer, thereby contributing to forming intense interfacial contact with the electrodes and higher reproducibility. In

addition, we also found that the $I_{ON2}/I_{ON1}/I_{OFF}$ ratio for CN-TBT based device is lower than that of ^tBu-TBT, which is consistent with the I - V test results. Then, the resistance switching threshold voltage distributions of TBT, CN-TBT, ^tBu-TBT and OMe-TBT based devices were also investigated. The distribution histogram and Gaussian fitting curves of the V_{th} values of all devices are displayed in **Figure S19**. It is obvious that these parameters are Gaussian distributed. For TBT and OMe-TBT based devices, the average V_{th} values are 1.70 ± 0.11 V and 1.39 ± 0.10 V, respectively. For CN-TBT based device, the V_{th1} and V_{th2} have an effective average value of 1.88 ± 0.13 V and 2.86 ± 0.18 V, respectively. For ^tBu-TBT based device, the V_{th1} and V_{th2} show similar distributions ($V_{th1} = 1.73 \pm 0.12$ V, $V_{th2} = 2.89 \pm 0.15$ V) with reasonably narrow standard deviations, further implying that this device has a good repeatability and parameter consistency. Moreover, the threshold voltages of ON1 state for both CN-TBT and ^tBu-TBT based devices have narrower distribution than that of ON2 state, which indicates that the ON1 states of the CN-TBT and ^tBu-TBT based devices are more stable and reproducible as compared to ON2 states.

Taking into account of the importance of the stability of switching phenomenon, the continuous voltage stress at 1 V for the OFF and ON states were applied to investigate the retention characteristic of devices (see **Figure 6(a-d)**). Obviously, a negligible change in current was observed for the OFF, ON1, and ON2 states even after 10^3 s of a constant application of 1 V of voltage, which suggests a high durability and a low error memory performance of all the devices. In order to further investigate the endurance ability of the ITO/molecule/Al memory devices, cyclic switching operations have been conducted, as shown in **Figure 6(e-h)**. It is obvious that all devices exhibit stable electrical performance during cycling sweep either in the HRS or the LRS, and no distinct degeneration was observed over 100 consecutive resistive switching cycles, again confirming that these memory devices have high reproducibility. The fluctuations of current appeared throughout the test, which may be caused by the instability of the material and the charge injection

process.^[42] We retested the I – V curves for all devices, as shown in **Figure S20**. It was found that all devices still keep the ON state even after one month, which strongly demonstrates the excellent stability and nonvolatility of these memory devices.

It has been reported that the Al electrode may diffuse into the active layer and participate in the formation of the conductive pathway during the vacuum deposition process.^[43–45] Therefore, the LiF layer (5 nm) was embedded between the organic active layer and top Al electrode to examine whether the ternary WORM memory behaviors of these devices are due to the metal filament conduction phenomenon or not. As shown in **Figure S21**, the I – V characteristics of memory devices within LiF layer are similar to those without LiF, indicating that conductivity changes are irrelevant to the metal filament. Moreover, when Al electrode was substituted by Au for ^tBu-TBT based memory device (the ^tBu-TBT layer has a thickness of 250 nm), the I – V characteristic was also unchanged, which further proves the irrelevancy of conductivity and formation of metal filament (**Figure S22**).

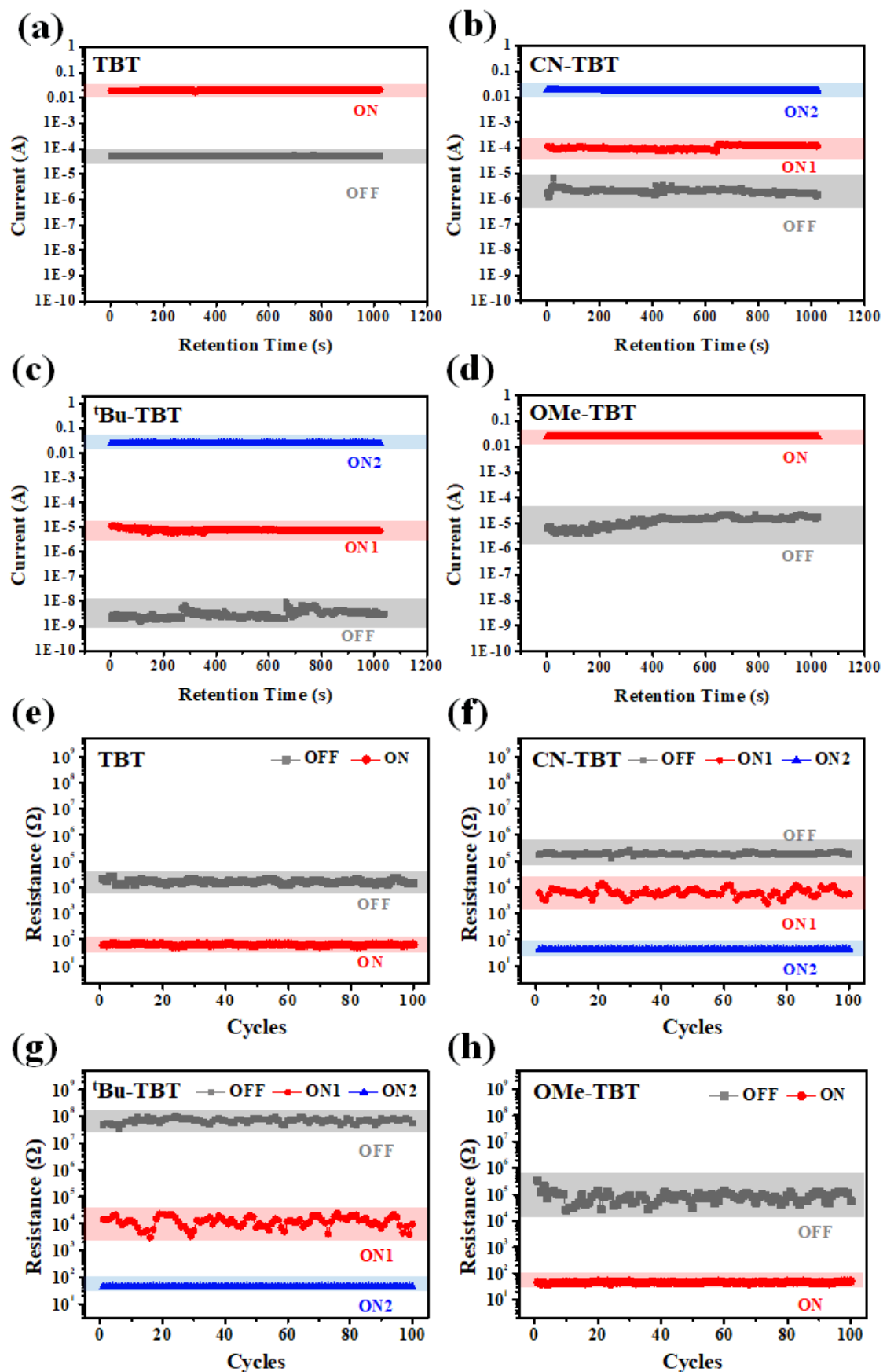


Figure 6 Retention characteristic of the memory devices based on ITO/molecule/Al under constant stress at 1 V for (a) TBT, (b) CN -TBT, (c) ^tBu-TBT, and (d) OMe -TBT, respectively.

Endurance ability tests of memory devices based on (e) TBT, (f) CN-TBT, (g) ^tBu-TBT, and (h) OMe-TBT for 100 cycles.

2.6. Morphology of the thin films

To investigate the influence of the microstructure of thin films on the performance of devices, the surface morphologies of thin films of TBT, ^tBu-TBT, CN-TBT and OMe-TBT were characterized by AFM. As shown in **Figure 7**, all four thin films show a relatively smooth surface, with the surface root-mean-square (RMS) values of 0.44, 1.07, 0.31 and 0.75 nm, respectively. This result indicates that TBT and ^tBu-TBT can be more favorable to form intense interfacial contact with the electrodes, which can effectively facilitate the charge injection from the electrode into the organic molecules and prevent the Al nanoparticles from penetrating into the film during the Al electrode deposition process. The much lower RMS of ^tBu-TBT relative to other films is mainly attributed to the steric hindrance of ^tBu groups, which reduces the direct π - π face-to-face interaction but maintains more π - π edge-to-face interactions, thereby leading to the increase of charge transport. In addition, it can be observed obviously that the surface defects (act as charge trapping sites) in the CN-TBT and OMe-TBT are much more than ^tBu-TBT. This would negatively influence the threshold voltage of the corresponding memory devices.^[46, 47]

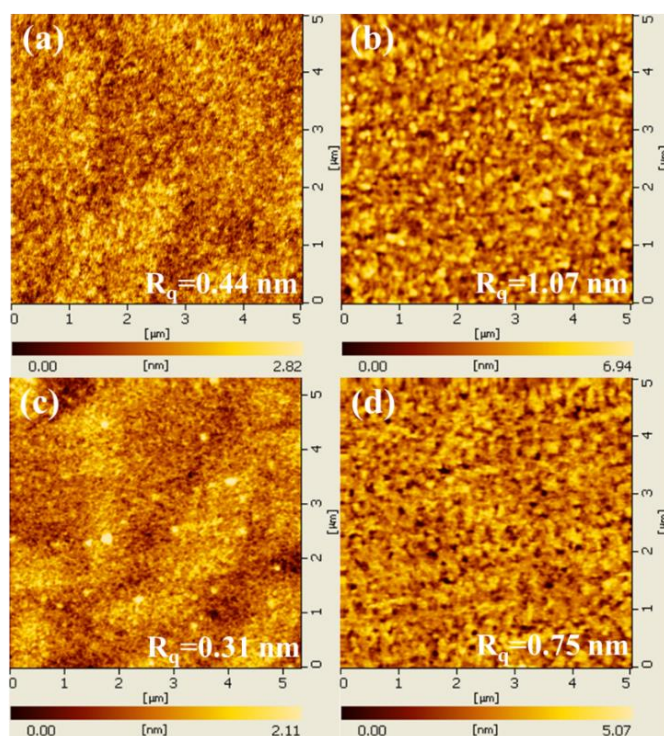


Figure 7 Tapping-mode AFM height images and typical cross-section profiles of AFM topographic images of thin films by thermal evaporation on ITO substrates: (a) TBT, (b) CN-TBT, (c) ^tBu-TBT, and (d) OMe-TBT.

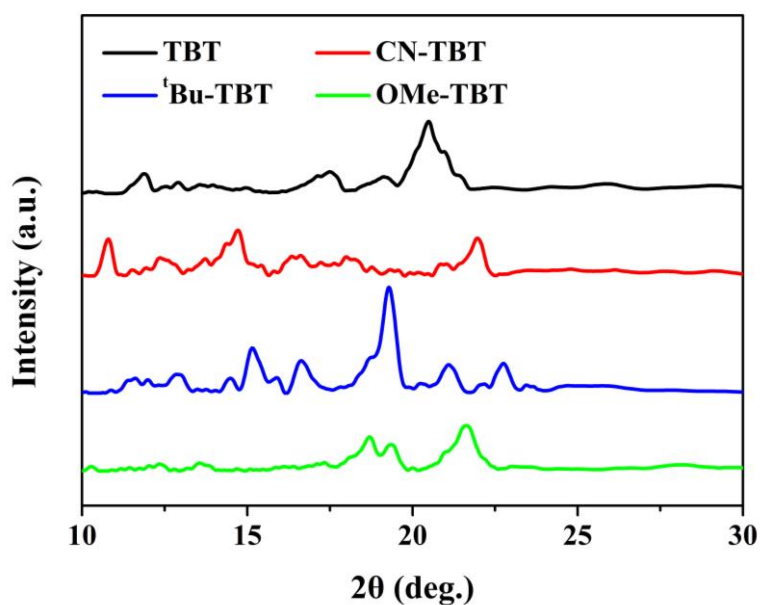


Figure 8 X-ray diffraction (XRD) patterns of TBT, CN-TBT, ^tBu-TBT, and OMe-TBT thin films on quartz substrates.

In order to confirm the crystal structures of the organic thin films, X-ray diffraction (XRD) spectra of the sublimed compounds were measured. As displayed in **Figure 8**, all molecules show high-intensity diffraction peaks, indicating the close packing between the neighboring molecules. The diffraction peaks at 20.50° for TBT, 21.92° for CN-TBT, 22.77° for ^tBu-TBT and 21.58° for OMe-TBT correspond to the π - π stacking distances of 4.33 Å, 4.05 Å, 3.90 Å and 4.11 Å, respectively.^[21, 48] This implies that the introduction of CN, ^tBu and OMe would benefit the molecular stacking and formation of ordered crystalline structure, thus facilitating the charge transport. Notably, the ^tBu-TBT compound shows the smallest π - π stacking distance. It was pointed out in the previous literature that the *tert*-butyl substituent can reduce direct π - π face-to-face interactions and maintain direct π - π edge-to-face interactions.^[29] So, it can be deduced that π - π face-to-face intermolecular interactions exist in CN-TBT and OMe-TBT, while ^tBu-TBT exhibits mainly C-H $\cdots\pi$ edge-to-face interactions, which contributes positively to both the formation of conducting channel and charge transport. This is also consistent with the observations from DSC. Based on the above results, we can conclude that altering the terminal moiety in D-A organic molecules could adjust their photophysical properties, molecular packing manner and memory performance.

2.7. Proposed data storage mechanism

To gain a better understanding of the switching models, the charge trapping and charge transfer switching mechanisms are proposed for the CN-TBT, ^tBu-TBT and OMe-TBT based devices. The I - V curve was well fitted to trap-controlled space charge limited current (SCLC) theoretical model. **Figure S23** shows the linear fitting in the logarithmic plots of the I - V curves of all devices. The trap-controlled SCLC describes the charge conduction via charge trapping, comprising of an ohmic regime ($I \propto V$) and a trap-limited SCLC regime ($I \propto V^2$). Under a low positive bias (about 0-0.6 V, first stage), the I - V curves of all devices can be elucidated by the ohmic conductance model ($I \propto V$). When the voltage increased (from about

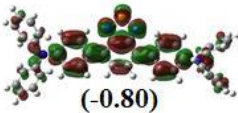
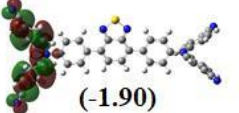
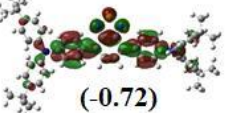
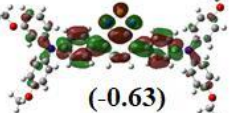
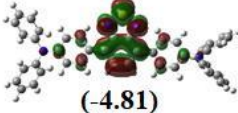
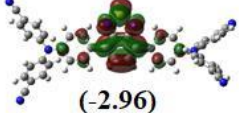
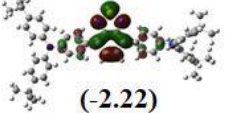
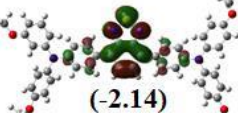
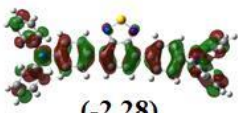
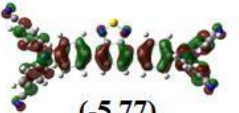

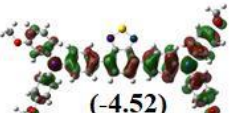
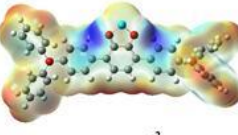
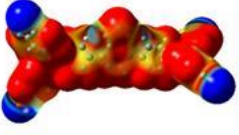
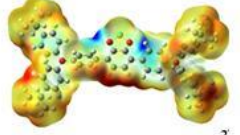
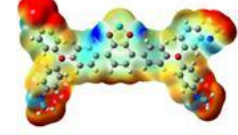

0.6 V to the threshold voltage, second stage), the Schottky barriers were formed which can block the partial charge injection. Afterwards, when the bias increased to higher than the Schottky barriers, holes began to inject and accumulate gradually near the anode. Then the SCLC model dominates in charge transport and the I - V curves follow the relationship of $I \propto V^2$. Meanwhile, the traps in the thin films were filled with injected charges at the high conductive state. The observation of an abrupt current increase at the switching threshold voltage indicates that the device underwent a sharp electrical transition from high-resistance state (OFF) to low-resistance state (ON for TBT and OMe-TBT, ON1 for CN-TBT and ^tBu-TBT). At the third stage from ON1 stage to ON2 stage, the slope of I - V curve for CN-TBT and ^tBu-TBT is approximately 2 and the conducting model fits well with the SCLC transport model. Different from CN-TBT and ^tBu-TBT, the slope of I - V curve for TBT and OMe-TBT is close to 1 and the conducting model could be fitted with the ohmic model. At the fourth stage (ON2 state), the I - V curves of CN-TBT and ^tBu-TBT changed to obey the ohmic model again.

In order to further explain the electrical switching behaviors of these memory devices, theoretical calculations were performed by the density functional theory (DFT) method at the B3LYP level using the 6-31G (d, p) basis set (as shown in **Table 3**).^[34] The calculation results indicate that the molecular surfaces have continuous positive ESP regions (red), which can act as open channels for the migration of charge carriers across the molecular backbone.^[37] The electron-deficient groups, such as -BT and -CN units, shown as the negative ESP regions (blue) can serve as “charge traps” to block the migration of charge carriers. The LUMOs of all molecules are mainly localized on the BT units, while the HOMOs are almost spread over the whole molecular backbone. The localization of HOMO/LUMO orbitals on the D-A moieties will guarantee the occurrence of ICT from the electron donor (TPA) to the acceptor (BT) and the nonvolatile memory characteristic, which could be explained by “charge-trapping” mechanism.^[20, 24] For all devices, when the external bias increased, the

shallower traps (HOMO of BT) will be firstly filled, resulting in current transition from the OFF to ON or ON1 state (corresponding to the HOMO to LUMO transition). It is known that the energetic depth of each trap in the molecules is consistent with the electron-withdrawing abilities of the substituent moieties. So for CN-TBT, the first threshold voltage (V_{th1}) increased obviously due to the strong electron-withdrawing ability of the -CN group. As the external voltage increased to the V_{th2} , the deeper charge traps (HOMO of CN) will be fully filled (corresponding to the HOMO to LUMO+1 transition), leading to the current transition from ON1 state to the ON2 state. For ^tBu-TBT, the specific steric effect of the -^tBu moiety can maintain the direct π - π edge-to-face interactions with shorter d-spacing distance and reduce direct π - π face-to-face interactions.^[49] This special molecular packing structure could facilitate the intermolecular CT from the whole ^tBu-TPA unit to the -BT group and benefit the formation of the second conducting channel, and thus, the ternary WORM data-storage behavior is established. To better illustrate the conducting mechanism of ^tBu-TBT based device, we drawn a cartoon schematic for the packed ^tBu-TBT molecules with H atoms omitted for clarity except for the benzothiadiazole core (see **Figure 9**). **Figure 9(a and b)** show the edge-to-face stacking mode of ^tBu-TBT molecules along the direction of top view and side view. When viewing along the side view direction, new channels of regular arrangement can be seen with H atoms of benzothiadiazole orienting to the neighboring molecules and pointing to the benzothiadiazole core. The direct π - π face-to-face interactions are reduced and more C-H $\cdots\pi$ edge-to-face interactions appeared due to the steric effect of *tert*-butyl groups. Due to the C-H $\cdots\pi$ edge-to-face interactions, the intermolecular charge transfer between the triphenylamine and benzothiadiazole was induced, leading to higher conductivity at a high applied voltage. Such channels can increase the carrier mobility anisotropically, and further reduce the turn-on voltage of the device.^[29,50] The high ON/OFF current ratio of ^tBu-TBT based device can be rationalized by the results of AFM and XRD measurements, which implies a more compact molecular packing of ^tBu-TBT in the film state.

For OMe-TBT, its memory device only displays a binary WORM behavior because of the unfavorable molecular packing with a large π - π stacking distance. However, due to the strong electron-donating property of -OMe group, the energy barrier between the work function of ITO electrode and organic layer is shrunk, so the threshold voltage of OMe-TBT based device is significantly decreased. Notably, the ON/OFF current ratio of OMe-TBT based device is higher as compared to that of TBT, which could be ascribed to the strong charge affinity of -OMe group as reported in literature and thereby the boosted hole transport ability.^[51] Therefore, by introducing different types of terminal moieties, the film morphology and trap depth of D-A molecules can be modulated simultaneously, thereby realizing multilevel electrical memory behavior with the lower threshold voltage and higher ON/OFF current ratio.

Table 3 DFT molecular simulation results (B3LYP/6-31G (d, p) level) of TBT, CN-TBT, ^tBu-TBT and OMe-TBT: HOMO, LUMO and ESP molecular orbitals.

Molecules	TBT	CN-TBT	^t Bu-TBT	OMe-TBT
LUMO+1 (eV)	 (-0.80)	 (-1.90)	 (-0.72)	 (-0.63)
LUMO (eV)	 (-4.81)	 (-2.96)	 (-2.22)	 (-2.14)
HOMO (eV)	 (-2.28)	 (-5.77)	 (-4.67)	 (-4.52)
ESP				
<div style="display: flex; align-items: center; justify-content: center;"> $-4.0e^{-2}$  $1.5e^{-2}$ </div>				

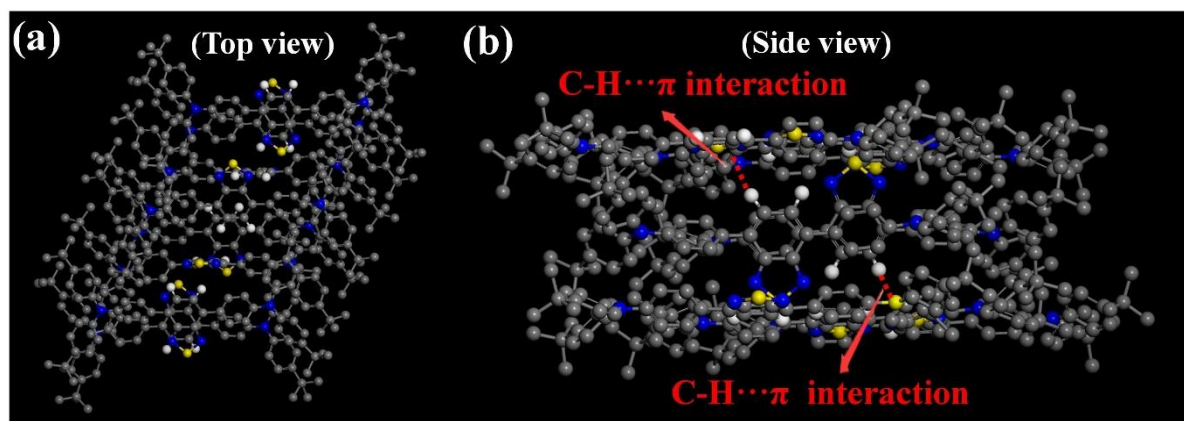


Figure 9 Cartoon schematic of the packed ^tBu-TBT molecules with H atoms omitted for clarity except for the benzothiadiazole core: (a) top view; (b) side view (Gray: C, blue: N, yellow: S and light gray: H).

3. Conclusion

Three new conjugated D-A small molecules with different types of substituent moieties on the molecular backbone of TBT (CN-TBT, ^tBu-TBT and OMe-TBT) were successfully designed and synthesized. The resulting memory devices based on CN-TBT and ^tBu-TBT exhibit excellent nonvolatile ternary WORM memory character, while those based on TBT and OMe-TBT only show binary WORM memory behavior. According to the analysis of the molecular orbital energy levels, film morphology, molecular packing arrangement as well as the DFT theoretical calculations, we can learn that the trap depth and molecular packing manner are responsible for the multilevel memory behavior rather than the numbers of electron-withdrawing units. The OMe-TBT based memory device exhibits the lowest operating voltage, and ^tBu-TBT based memory device shows the highest I_{ON}/I_{OFF} ratio. The performance of ^tBu-TBT based device is superior to that of the CN-TBT based device, revealing that introduction of the electron-donating groups with specific steric effect and appropriate electron affinity can modulate the molecular packing motif, thin film morphological structure and trap depth simultaneously, thereby realizing excellent memory performance. These results may provide new strategies for further exploration of the high performance organic resistive memory devices.

4. Experimental Section

Materials: All chemicals and reagents were purchased from commercial sources and used without further purification. 4,7-Dibromobenzo[c]-1,2,5-thiadiazole, tetrakis(triphenylphosphine)palladium, 4-(diphenylamino)phenylboronic acid, potassium carbonate, potassium iodide, potassium iodate, bis(pinacolato)diboron, [1,1'-bis(diphenylphosphino)ferrocene]dichloropalladium(II), potassium acetate, 4-iodoaniline, 4-fluorobenzonitrile, caesium fluoride, iodobenzene, potassium *tert*-butanolate, tri-*tert*-butylphosphine, palladium diacetate, 4,4'-dimethoxydiphenylamine, N-iodosuccinimide, potassium hydroxide and 4-(*tert*-butyl)-N-(4-(*tert*-butyl)phenyl)-N-(4-iodophenyl)aniline were all purchased from Energy Chemical Co.. Separation or purification of the products was achieved by column chromatography using silica gel (200–300 mesh). All reactions were carried out under nitrogen unless otherwise stated.

Synthesis of TBT. 4,7-Dibromobenzo[c]-1,2,5-thiadiazole (250 mg, 0.85 mmol), 4-(diphenylamino)phenylboronic acid (542 mg, 1.90 mmol), and Pd(PPh₃)₄ (50 mg, 0.04 mmol) were placed in a 100 mL three-necked flask under a N₂ atmosphere. Then a solution of K₂CO₃ (550 mg, 4 mmol) in deionized water (5 mL) was added. Anhydrous 1,2-dimethoxyethane (30 mL) was added into the mixture. The reaction mixture was heated to 85 °C for 8 h. After completion of the reaction, the reaction mixture was poured slowly into a separatory funnel and extracted with DCM. Then the combined extracts were dried over anhydrous Mg₂SO₄ and the solvent was removed under reduced pressure. The residue was finally purified by using silica gel column chromatography with petroleum ether and DCM as the eluent to give the final product as an orange solid (300 mg, 56 %). ¹H NMR (600 MHz, chloroform-*d*, δ): 7.88 (d, *J* = 8.8 Hz, 4H), 7.74 (s, 2H), 7.28 (t, *J* = 8 Hz 8H), 7.22 – 7.18 (m, 12H), 7.06 (t, *J* = 7.4 Hz, 4H); ¹³C NMR (151 MHz, chloroform-*d*, δ): 154.37, 148.19, 147.71, 132.36, 131.23, 130.07, 129.50, 127.54, 125.07, 123.46, 123.11; MALDI-TOF: *m/z* calcd for: 622.219; found: 622.204 [M]⁺.

Synthesis of CN-TBT. 4,7-Bis(4,4,5,5-tetramethyl-1,3,2-dioxaborolan-2-yl)benzo[c][1,2,5]thiadiazole (390 mg, 1 mmol), 4,4'-((4-iodophenyl)azanediyl)dibenzonitrile (930 mg, 2.20 mmol), and Pd(PPh₃)₄ (122 mg, 0.11 mmol) were placed in a 100 mL three-necked flask. Then a solution of K₂CO₃ (910 mg, 6.50 mmol) in deionized water (5 mL) was added. Anhydrous THF (30 mL) was added into the system. The reaction mixture was heated to 65 °C for 8 h. After completion of the reaction, the reaction mixture was poured slowly into a separatory funnel and extracted with DCM. Then the combined extracts were dried over anhydrous Mg₂SO₄ and the solvent was removed under reduced pressure. The residue was similarly purified by using column chromatography with petroleum ether and DCM as the eluent to give rise to the CN-TBT as a yellow solid (339 mg, 47 %). ¹H NMR (600 MHz, chloroform-*d*, δ): 8.04 (d, *J* = 8.8 Hz, 4H), 7.83 (s, 2H), 7.58 (d, *J* = 8.9 Hz, 8H), 7.30 (d, *J* = 8.7 Hz, 4H), 7.22 (d, *J* = 8.9 Hz, 8H); ¹³C NMR (151 MHz, chloroform-*d*, δ): 154.00, 150.14, 145.34, 135.02, 133.79, 132.30, 131.06, 128.17, 126.54, 123.55, 118.91, 106.46; MALDI-TOF: *m/z* calcd for: 722.200; found: 722.224 [M]⁺.

Synthesis of ^tBu-TBT. Compound ^tBu-TBT was synthesized by the same procedure as described above for CN-TBT by using 4,7-bis(4,4,5,5-tetramethyl-1,3,2-dioxaborolan-2-yl)benzo[c][1,2,5]thiadiazole and 4,4'-((4-iodophenyl)methylene)bis(*tert*-butylbenzene) as the starting materials. The ^tBu-TBT was finally obtained as an orange solid (172 mg, 29 %). ¹H NMR (600 MHz, chloroform-*d*, δ): 7.85 (d, *J* = 8.8 Hz, 4H), 7.73 (s, 2H), 7.30 (d, *J* = 8.7 Hz, 8H), 7.19 (d, *J* = 8.7 Hz, 4H), 7.12 (d, *J* = 8.7 Hz, 8H), 1.33 (s, 36H); ¹³C NMR (151 MHz, chloroform-*d*, δ): 154.34, 146.26, 132.26, 129.85, 127.40, 126.26, 124.66, 122.19, 34.48, 31.61, 1.18; MALDI-TOF: *m/z* calcd for: 846.470; found: 846.588 [M]⁺.

Synthesis of OMe-TBT. Compound OMe-TBT was synthesized by the same procedure as described above for CN-TBT by using 4,7-bis(4,4,5,5-tetramethyl-1,3,2-dioxaborolan-2-yl)benzo[c][1,2,5]thiadiazole and 4-iodo-*N,N*-bis(4-methoxyphenyl)aniline as the starting materials. The OMe-TBT was finally obtained as a red solid (82 mg, 22 %). ¹H NMR (600

MHz, chloroform-*d*, δ): 7.81 (d, J = 8.8 Hz, 4H), 7.69 (s, 2H), 7.14 (d, J = 8.9 Hz, 8H), 7.06 (d, J = 8.8 Hz, 4H), 6.86 (d, J = 9.0 Hz, 8H), 3.81 (s, 12H); ^{13}C NMR (151 MHz, chloroform-*d*, δ): 156.22, 154.35, 148.91, 140.72, 132.15, 129.81, 129.23, 127.22, 127.12, 119.95, 114.88, 55.64; MALDI-TOF: m/z calcd for: 742.261; found: 742.291 $[\text{M}]^+$.

Characterization of compounds: ^1H and ^{13}C NMR spectra were recorded in CDCl_3 on a Bruker DRX400 instrument or Bruker DRX600 instrument with a tetramethylsilane (TMS) as a reference for the chemical shifts. Fourier transform infrared (FTIR) spectra were recorded on a Bruker TENSOR 27 spectrophotometer using KBr pellets for solid state spectroscopy. Matrix Assisted Laser Desorption Ionization-Time of Flight Mass Spectra (MALDI-TOF MS) were carried out on Bruker ultraflex MALDI-TOF/TOF. Thermogravimetric analysis (TGA) and differential scanning calorimeter (DSC) were performed with a TGA-700 and DSC PT1000 at a heating rate of 10 $^\circ\text{C}/\text{min}$ under a N_2 atmosphere (flowing rate of 50 mL/min), respectively. The UV-vis absorption spectra were recorded on a Hitachi U-3900 spectrophotometer at room temperature. Photoluminescence (PL) spectra were recorded on an Edinburgh FLS980 spectrometer at room temperature. The cyclic voltammetry (CV) experiments were performed by using a CHI600E electrochemical workstation with a common three-electrode cell consisting of a glassy carbon working electrode, a Pt wire auxiliary electrode, and a regular calomel reference electrode in saturated KCl solution. The oxidation and reduction potentials were measured in 0.1 M CH_3CN solution of tetrabutylammonium hexafluorophosphate (TBAPF_6) at a scan rate of 100 mV/s. Atomic force microscopy (AFM) measurements were performed by using a SPA-300HV AFM instrument. X-ray diffraction (XRD) analysis was obtained on a Bruker D8 Advance with a $\text{Cu K}\alpha$ monochromatic radiation source.

Fabrication and measurements of memory devices: The memory devices with the sandwich-like structure of ITO/active layer/Al were fabricated through thermal evaporation technique. The indium tin oxide (ITO) conductive glasses with the size of 20 mm \times 20 mm were pre-

cleaned successively with acetone, ultraclean water, and isopropanol in an ultrasonic bath for 25 min. Then ITO substrates were put into an evaporation chamber. The active layer (80 nm) and top aluminum (Al) electrodes (150 nm) were evaporated through a shadow mask ($\phi = 300\ \mu\text{m}$) onto ITO surface at 2.5×10^{-4} Torr. In addition, the LiF layer (5 nm) in the reference devices was deposited under the same conditions. Current-voltage (I - V) characteristics of all the memory devices were measured with 4200SCS power source equipped with a probe station. The interval time of every sweep is 30 min after the voltage is turned off. All electrical measurements of the devices were taken under ambient conditions.

Supporting Information

Supporting Information is available from the Wiley Online Library or from the author.

Acknowledgements

We acknowledge the financial support from the National Natural Science Foundation of China (Grant No.: 61774109). This work was also supported by the Youth “Sanjin” Scholar Program, the Key R&D Project of Shanxi Province (International cooperation program, No. 201603D421032), and the Natural Science Foundation of Shanxi Province (Grant No.: 201801D211007). Yongquan Qu also thanks the Hundred Talents Program of Shanxi Province for the financial support. W.-Y.W. thanks the financial support from the Science, Technology and Innovation Committee of Shenzhen Municipality (JCYJ20180507183413211), the Hong Kong Research Grants Council (PolyU 123384/16P), Hong Kong Polytechnic University (1-ZE1C) and Ms Clarea Au for the Endowed Professorship in Energy (847S). Jinba Han and Hong Lian contribute equally to this work.

Received: ((will be filled in by the editorial staff))

Revised: ((will be filled in by the editorial staff))

Published online: ((will be filled in by the editorial staff))

References

- [1] J. Lee, E. Lee, S. Kim, G. S. Bang, D. A. Shultz, R. D. Schmidt, M. D. E. Forbes, H. Lee, *Angew. Chem. Int. Ed.* **2011**, *50*, 4414.
- [2] G. Y. Jiang, T. Michinobu, W. F. Yuan, M. Teng, Y. Q. Wen, S. X. Du, H. J. Gao, L. Jiang, Y. L. Song, F. Diederich, D. B. Zhu, *Adv. Mater.* **2005**, *17*, 2170.
- [3] J. C. Scott, L. D. Bozano, *Adv. Mater.* **2007**, *19*, 1452.

- [4] H. Jiang, H. P. Zhao, K. K. Zhang, X. D. Chen, C. Kloc, W. P. Hu, *Adv. Mater.* **2011**, *23*, 5075.
- [5] D. Xiang, X. Wang, C. Jia, T. Lee, X. Guo, *Chem. Rev.* **2016**, *116*, 4318.
- [6] C. W. Chu, J. Ouyang, J. H. Tseng, Y. Yang, *Adv. Mater.* **2005**, *17*, 1440.
- [7] Y. L. Shang, Y. Q. Wen, S. L. Li, S. X. Du, X. B. He, L. Cai, Y. F. Li, L. M. Yang, H. J. Gao, Y. L. Song, *J. Am. Chem. Soc.* **2007**, *129*, 11674.
- [8] Y. Yonekuta, K. Susuki, K. Oyaizu, K. Honda, *J. Am. Chem. Soc.* **2007**, *129*, 14128.
- [9] Y. Sun, D. Wen, *Prog. Org. Coat.* **2020**, *142*, 105613.
- [10] Y. Sun, D. Wen, *J. Alloys Compd.* **2019**, *806*, 215.
- [11] Y. Sun, D. Wen, F. Sun, *Org. Electron.* **2019**, *65*, 141.
- [12] M. Ochiai, N. Tada, T. Okada, A. Sota and K. Miyamoto, *J. Am. Chem. Soc.* **2008**, *130*, 2118.
- [13] J. Liu, Z. Zeng, X. Cao, G. Lu, L.-H. Wang, Q.-L. Fan, W. Huang and H. Zhang, *Small* **2012**, *8*, 3517.
- [14] T.-W. Kim, H. Choi, S.-H. Oh, G. Wang, D.-Y. Kim, H. Hwang and T. Lee, *Adv. Mater.* **2009**, *21*, 2497.
- [15] C. Wang, P. Gu, B. Hu and Q. Zhang, *J. Mater. Chem. C* **2015**, *3*, 10055.
- [16] S. Gao, X. Yi, J. Shang, G. Liu, R. W. Li, *Chem. Soc. Rev.* **2019**, *48*, 1531.
- [17] Q. F. Gu, J. H. He, D. Y. Chen, H. L. Dong, Y. Y. Li, H. Li, Q. F. Xu, J. M. Lu, *Adv. Mater.* **2015**, *27*, 5968.
- [18] H. Zhuang, Q. Zhang, Y. Zhu, X. Xu, H. Liu, N. Li, Q. Xu, H. Li, J. Lu, L. Wang, *J. Mater. Chem. C* **2013**, *1*, 3816.
- [19] Q. Bao, Q. Zhang, Y. Li, H. Li, J. He, Q. Xu, N. Li, D. Chen, J. Lu, *Org. Electron.* **2016**, *28*, 155.
- [20] L. Hua, X. Qingfeng, L. Najun, S. Ru, G. Jianfeng, L. Jianmei, G. Hongwei, Y. Feng, *J. Am. Chem. Soc.* **2010**, *132*, 5542.

- [21] S. Miao, Y. Zhu, H. Zhuang, X. Xu, H. Li, R. Sun, N. Li, S. Ji, J. Lu, *J. Mater. Chem. C* **2013**, *1*, 2320.
- [22] Q. Zhang, J. He, H. Zhuang, H. Li, N. Li, Q. Xu, D. Chen, J. Lu, *Adv. Funct. Mater.* **2016**, *26*, 146.
- [23] W. Ren, H. Zhuang, Q. Bao, S. Miao, H. Li, J. Lu and L. Wang, *Dyes Pigm.* **2014**, *100*, 127.
- [24] Q. Bao, H. Li, Y. Li, J. He, Q. Xu, N. Li, D. Chen, L. Wang, J. Lu, *Dyes Pigm.* **2016**, *130*, 306.
- [25] Z. Liu, E. Shi, Y. Wan, N. Li, D. Chen, Q. Xu, H. Li, J. Lu, K. Zhang, L. Wang, *J. Mater. Chem. C* **2015**, *3*, 2033.
- [26] H. Liu, H. Zhuang, H. Li, J. Lu, L. Wang, *Phys. Chem. Chem. Phys.* **2014**, *16*, 17125.
- [27] X. Chen, Z. Yang, W. Li, Z. Mao, J. Zhao, Y. Zhang, Y.-C. Wu, S. Jiao, Y. Liu, Z. Chi, *ACS Appl. Mater. Interfaces* **2019**, *11*, 39026.
- [28] J. Lu, J. Yuan, W. Guo, X. Huang, Z. Liu, H. Zhao, H.-Q. Wang, W. Ma, *Polym. Chem.* **2014**, *5*, 4772.
- [29] J. Keruckas, D. Volyniuk, J. Simokaitiene, E. Narbutaitis, A. Lazauskas, P.-H. Lee, T.-L. Chiu, C.-F. Lin, P. Arsenyan, J.-H. Lee, J. V. Grazulevicius, *Org. Electron.* **2019**, *73*, 317.
- [30] S. Pu, C. Fan, W. Miao, G. Liu, *Dyes Pigm.* **2010**, *84*, 25.
- [31] M. Wałęsa-Chorab, W. G. Skene, *ACS Appl. Mater. Interfaces* **2017**, *9*, 21524.
- [32] G. Grybauskaite-Kaminskiene, D. Volyniuk, V. Mimaite, O. Bezikonny, A. Bucinskas, G. Bagdziunas, J. V. Grazulevicius, *Chem. - Eur. J.* **2018**, *24*, 9581.
- [33] S.-i. Kato, T. Matsumoto, M. Shigeiwa, H. Gorohmaru, S. Maeda, T. Ishi-I, S. Mataka, *Chem. - Eur. J.* **2006**, *12*, 2303.
- [34] T. Ishi-i, N. Nakamura, S. Amemori, K. Kasatani, H. Gorohmaru, M. Ishida, M. Shigeiwa, *Dyes Pigm.* **2013**, *99*, 14.

- [35] R. Balasaravanan, V. Sadhasivam, A. Siva, M. Pandi, G. Thanasekaran, C. Arulvasu, *ChemistrySelect* **2016**, *1*, 2792.
- [36] C. B. Larsen, H. van der Salm, G. E. Shillito, N. T. Lucas, K. C. Gordon, *Inorg. Chem.* **2016**, *55*, 8446.
- [37] P.-Y. Gu, F. Zhou, J. Gao, G. Li, C. Wang, Q.-F. Xu, Q. Zhang, J.-M. Lu, *J. Am. Chem. Soc.* **2013**, *135*, 14086.
- [38] H. Fang, H. Gao, T. Wang, B. Zhang, W. Xing, X. Cheng, *Dyes Pigm.* **2017**, *147*, 190.
- [39] G. L. Eakins, J. S. Alford, B. J. Tiegs, B. E. Breyfogle, C. J. Stearman, *J. Phys. Org. Chem.* **2011**, *24*, 1119.
- [40] Y.-C. Lai, F.-C. Hsu, J.-Y. Chen, J.-H. He, T.-C. Chang, Y.-P. Hsieh, T.-Y. Lin, Y.-J. Yang, Y.-F. Chen, *Adv. Mater.* **2013**, *25*, 2733.
- [41] Z. Li, Q. Zhang, C. Zhang, H. Li and J. Lu, *Org. Electron.* **2019**, *66*, 70.
- [42] K. Onlaor, T. Thiawong and B. Tunhoo, *J. Alloys Compd.* **2018**, *732*, 880.
- [43] Y. Li, H. Li, H. Chen, Y. Wan, N. Li, Q. Xu, J. He, D. Chen, L. Wang, J. Lu, *Adv. Funct. Mater.* **2015**, *25*, 4246.
- [44] H. Liu, R. Bo, H. Liu, N. Li, Q. Xu, H. Li, J. Lu, L. Wang, *J. Mater. Chem. C* **2014**, *2*, 5709.
- [45] P.-Y. Gu, J. Gao, C.-J. Lu, W. Chen, C. Wang, G. Li, F. Zhou, Q.-F. Xu, J.-M. Lu, Q. Zhang, *Mater. Horiz.* **2014**, *1*, 446.
- [46] B. Cho, S. Song, Y. Ji, T.-W. Kim, T. Lee, *Adv. Funct. Mater.* **2011**, *21*, 2806.
- [47] X.-D. Zhuang, Y. Chen, G. Liu, B. Zhang, K.-G. Neoh, E.-T. Kang, C.-X. Zhu, Y.-X. Li, L.-J. Niu, *Adv. Funct. Mater.* **2010**, *20*, 2916. H. Hu, J. He, H. Zhuang, E. Shi, H. Li, N. Li, D. Chen, Q. Xu, J. Lu and L. Wang, *J. Mater. Chem. C* **2015**, *3*, 8605.
- [48] H. Hu, J. He, H. Zhuang, E. Shi, H. Li, N. Li, D. Chen, Q. Xu, J. Lu and L. Wang, *J. Mater. Chem. C* **2015**, *3*, 8605.

- [49] K. Stalindurai, A. Karuppasamy, J.-D. Peng, K.-C. Ho, A. Tamilselvan, C. Ramalingan, *Tetrahedron* **2017**, 73, 278.
- [50] W.-S. Han, H.-J. Son, K.-R. Wee, K.-T. Min, S. Kwon, I.-H. Suh, S.-H. Choi, D. H. Jung and S. O. Kang, *J. Phys. Chem. C* **2009**, 113, 19686.
- [51] B. J. Ree, T. Isono, T. Satoh, *ACS Appl. Mater. Interfaces* **2020**, 12, 28435.